IOPscience iopscience.iop.org

Home Search Collections Journals About Contact us My IOPscience

Electronic states in faceted Au(111) studied with curved crystal surfaces

This article has been downloaded from IOPscience. Please scroll down to see the full text article.

2009 J. Phys.: Condens. Matter 21 353001

(http://iopscience.iop.org/0953-8984/21/35/353001)

View the table of contents for this issue, or go to the journal homepage for more

Download details:
IP Address: 129.252.86.83
The article was downloaded on 29/05/2010 at 20:48

Please note that terms and conditions apply.

J. Phys.: Condens. Matter **21** (2009) 353001 (15pp) doi:10.1088/0953-8984/21/35/353001

TOPICAL REVIEW

Electronic states in faceted Au(111) studied with curved crystal surfaces

M Corso[1], F Schiller[2], L Fernández[1], J Cordón[3] and J E Ortega[1,2,3,4]

[1] DIPC, Manuel Lardizábal 4, E-20018 San Sebastián, Spain
[2] Centro de Física de Materiales Centro Mixto (CSIC/UPV-EHU), Materials Physics Center—MPC, Manuel Lardizábal 3, E-20018 San Sebastián, Spain
[3] Departamento Física Aplicada I, Universidad del País Vasco, Plaza Oñate 2, E-20018 San Sebastián, Spain

E-mail: enrique.ortega@ehu.es

Received 9 March 2009, in final form 28 June 2009
Published 20 July 2009
Online at stacks.iop.org/JPhysCM/21/353001

Abstract

Vicinal Au(111) surfaces exhibit periodic faceting within a wide range of miscut angles. There, the system segregates two alternating phases with different step lattice constants d_w and d_n. Using a curved crystal surface that allows a smooth variation of the surface orientation, we have studied, as a function of the miscut angle, the evolution of Au(111) faceted structures by scanning tunneling microscopy, and their electronic surface states by angle-resolved photoemission. We observe that surface bands reflect the two-phase character of the faceted system, i.e. we find d_w- and d_n-like states that evolve accordingly to the faceted structure. Using a photoemission calculation we prove that the apparently complex topology hides relatively simple physics, i.e. the same free-electron-like dispersion and repulsive step scattering that feature surface bands in stepped noble metal surfaces. On the grounds of such simulations, we discuss the possible interference of the electronic energy in the delicate free energy balance that determines the critical size of reconstructed (d_w) and unreconstructed (d_n) terraces during Au faceting.

(Some figures in this article are in colour only in the electronic version)

Contents

[4] Author to whom any correspondence should be addressed.

1. Introduction

Vicinal surfaces with periodic arrays of steps and terraces are among the simplest lateral nanostructures. They are attractive as playgrounds for testing the fundamental properties of electrons at one- or two-dimensional (1D or 2D) superlattices [1–5], such as wavefunctions [6, 7], and useful as growth templates for self-assembled arrays of nanostructures [7–11]. The vicinal surface is simply defined by the tilt angle, or miscut α, with respect to the high symmetry direction of the terrace, which determines the average step–step distance (terrace width) d. In fact, for monatomic height h

 © 2009 IOP Publishing Ltd Printed in the UK

steps, which is the common case in metals, d is simply related to α by $d = h/\sin\alpha$. This equation reflects the ability to readily convert controllable macroscopic angles in the range of $\alpha \sim 1°$–$15°$ into nanoscopic superlattice constants d from ∼100 Å down to ∼10 Å, thereby making vicinal surfaces convenient growth templates and model superlattices.

Step edges behave as potential barriers for surface electrons [12]. In vicinal noble metal surfaces with step arrays scattering at steps gives rise to a rich surface electronic structure and phenomena that depend on the superlattice constant d. For example, the Shockley-like surface state that characterizes these surfaces is observed to evolve from a quasi-one-dimensional (1D) state to a two-dimensional (2D) band as a function of d [1, 2]. In fact, vicinal surfaces with relatively wide (111) terraces exhibit a large step potential, such that surface states get confined within individual terraces. As terraces become narrower the step barrier strength is reduced, allowing surface states to couple from terrace to terrace, leading to Shockley-like superlattice bands. This d-dependent variation in the step potential has been traced to the smooth transformation of surface states into resonances, as the bulk bandgap projected onto the surface plane, which supports surface states, vanishes away from the (111) direction [1, 2]. In any case, in a vicinal noble metal surface the characteristic free-electron-like band of the (111) plane appears broken up in a series of discrete states or minibands, leading to a surface state occupation and electronic energy that varies as a function of d.

Shockley states in noble metal surfaces are characterized by Fermi wavelengths $\lambda_F/2$ in the range of 15–40 Å [13]. Such long $\lambda_F/2$ values make (111)-oriented noble metal surfaces potential candidates to host charge density wave (CDW)-like instabilities [14]. These have not been observed on bare surfaces, but they have been proved to exist in overlayers and superlattices [3, 15, 16]. In the Ag/Cu(111) system the incommensurability and the extra atomic compression of the Ag monolayer (ML) is apparently connected to the presence of a surface CDW [16]. In fact, the Fermi surface in this system is nested and gapped at the $\bar{M}$ point of the surface Brillouin zone. CDW instabilities can be induced in noble metal surfaces with 1D or 2D arrays of scatterers by selecting the superlattice constant d that nests the Fermi surface. This allows one to straightforwardly explore the nature of the structural changes that arise when nesting conditions are approached. One good example is that of Ce atoms evaporated on Ag(111) at 4 K [15]. With the appropriate Ce atom concentration one can tune a 2D CDW, which in turn induces the formation of a structurally perfect 2D atom superlattice. In vicinal Cu(111) surfaces, 1D Fermi surface nesting can be forced by selecting the step lattice vector that exactly matches the Fermi wavelength $d = \lambda_F/2$ [3]. However, d is fixed by the crystal orientation of the surface, and hence the structural instability associated with the 1D Fermi surface nesting is not clear yet. The case of Au(111) vicinals is the reverse. The structural instabilities of the step superlattice are known, namely the two-phase separation or faceting that affects a characteristic range of miscuts (∼4°–10°) [8], but not the electronic states changes around the faceting transition. The question is whether or not the faceting instability is linked to a surface CDW that could be present in the system.

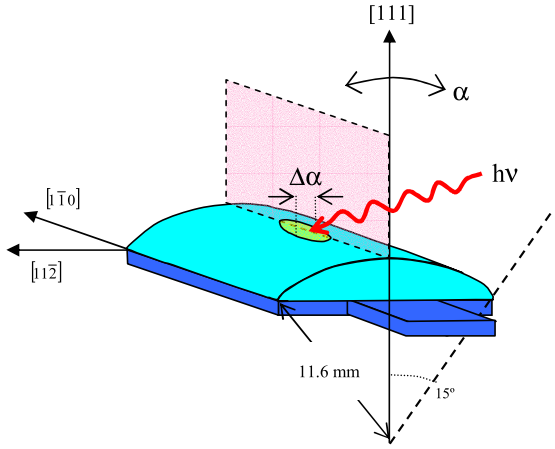

Figure 1. Schematic description of the curved Au(111) surface and geometry of the spatially resolved ARPES experiment carried out in the present work. Different surface orientations (α) and step types (positive and negative α) can be selected around the (111) direction (center). The sample is oriented with the incidence and the emission planes parallel and perpendicular to the [$\bar{1}$10] direction, respectively. The size of the light spot along [11$\bar{2}$] samples a finite miscut range $\Delta\alpha$.

Curved crystal surfaces, such as the one sketched in figure 1, allow a smooth variation of the miscut angle in the same sample, and hence appear as the rational way to explore physical and chemical properties of vicinal surfaces that depend on d. Curved crystal substrates were already used in the past to determine the role of steps in the chemisorption of water and oxygen on semiconductor surfaces [17], as well as to unveil the fundamental contribution of surface steps to the magnetic anisotropy in thin ferromagnetic films [18]. Using curved noble metal surfaces we generally want to investigate the dependence of surface states on the lattice constant d. In particular, we use them to check the existence of any structural/electronic interplay near the 1D Fermi surface nesting $d = \lambda_F/2$, which can be approached and accurately tuned in a curved sample.

In the present study we focus on the case of Au(111). First, we combine scanning tunneling microscopy (STM) and angle-resolved photoemission (ARPES) to obtain a thorough description of the geometry and the electronic states as a function of α using a curved Au(111) crystal. We precisely delimit the faceting range, where we measure the characteristic terrace sizes d_w and d_n for the two phases. Second, we complete our previous ARPES work on flat vicinals [2] and B-type steps [19] by extending the detailed analysis of the surface states to A-type steps. Our ARPES data prove that the surface band splits into low and high energy states for d_w and d_n phases, respectively, in both A- and B-type steps, although only A-type steps exhibit coherent electronic coupling between phases. Finally, we deepen in the theoretical model introduced in our previous work to simulate and analyze the photoemission data [19] by expressly calculating the surface band occupation and the electronic energy for different step configurations. This complete analysis allows us to

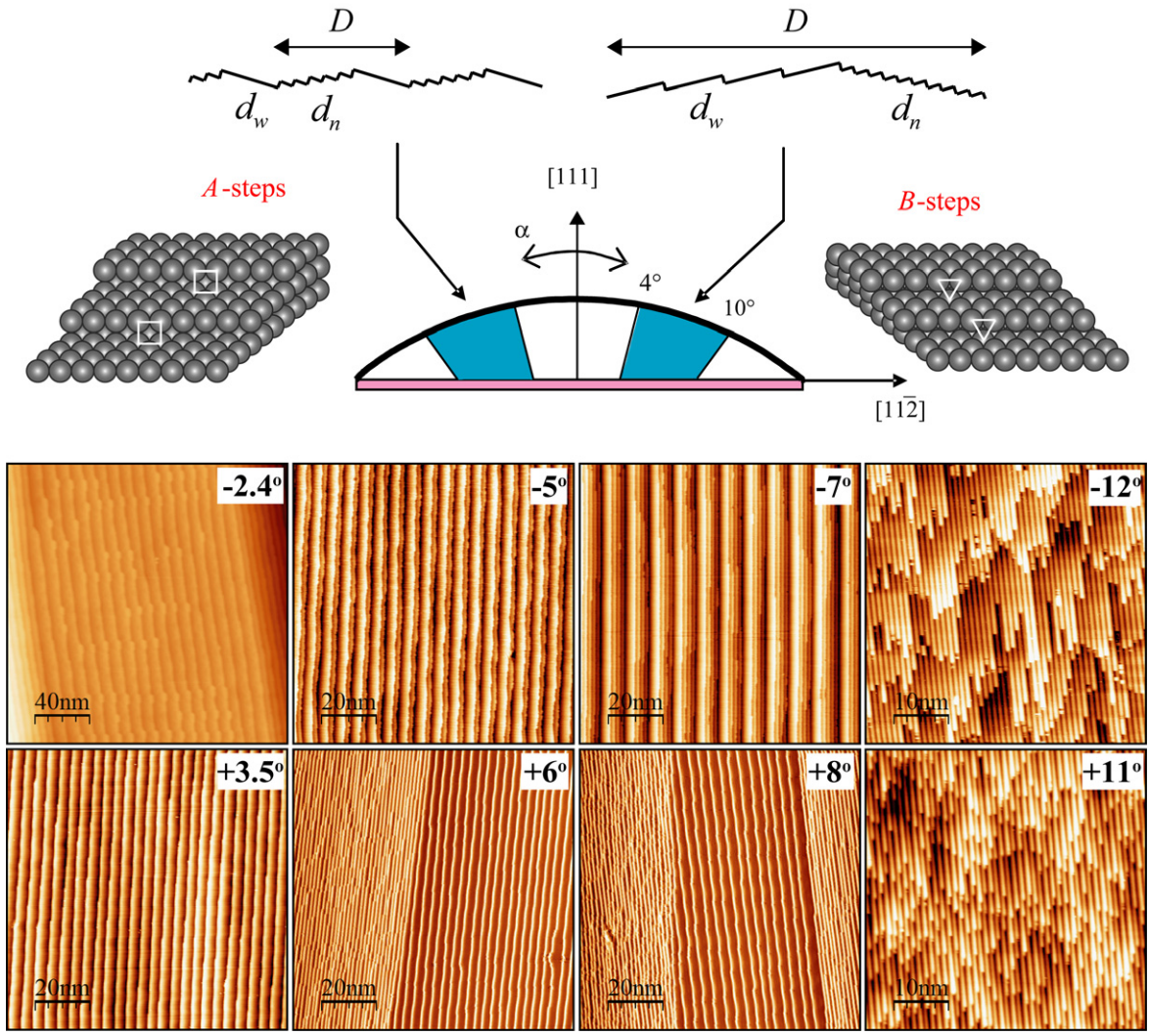

Figure 2. Top, schematic sideview of the Au(111) curved crystal, indicating the faceted areas. Faceting occurs within ∼4°–10° miscuts for both A and B sides, although the faceted structure is different in each case. The different atomic packing for A and B steps is also sketched. Bottom, STM images (topography or current) taken at different positions on the curved crystal as indicated. Negative miscut angles indicate A-type steps.

discuss in more detail the possible existence of electronic state instabilities that may have an influence, or even trigger the faceting transition.

2. Experimental results

The curved Au crystal (Mateck GmbH, Germany) was mechanically polished defining a $\alpha = \pm 15°$ cylindrical section (11.6 mm radius) around the [111] direction ($\alpha = 0°$). As depicted on top of figure 2, left and right sides of the crystal correspond to A-({100}-oriented microfacets) and B-type steps ({11$\bar{1}$} microfacets), respectively. The curved surface is prepared in vacuum following the standard ion sputtering plus annealing cycling used for flat crystals. In order to minimize surface damage, ion sputtering is carried out with the incidence plane parallel to the surface steps. We have observed that an extensive sputtering treatment perpendicular to the steps can significantly alter the curvature of the crystal. The local surface structure is determined with STM using a variable temperature set-up (Omicron). STM data have been analyzed using the WSXM software [20]. Locally resolved surface bands are measured with ARPES using synchrotron light from the PGM beamline of the Synchrotron Radiation Center (SRC) in Stoughton (WI). For ARPES we used a hemispherical Scienta SES200 spectrometer with energy and angular resolution set to 25 meV and 0.1°, respectively, and p-polarized light with the polarization plane parallel to surface steps, as shown in figure 1. STM experiments were carried out at 300 K, whereas ARPES measurements were performed at 150 K.

2.1. Structural analysis of the curved Au(111) surface

At the bottom of figure 2 we show characteristic STM images taken across the curved Au(111) surface at both the right side (positive α) and the left side (negative α) of the crystal. The structures are similar to those observed in regular vicinal Au(111) crystals with the same α angle [8]. In the faceted

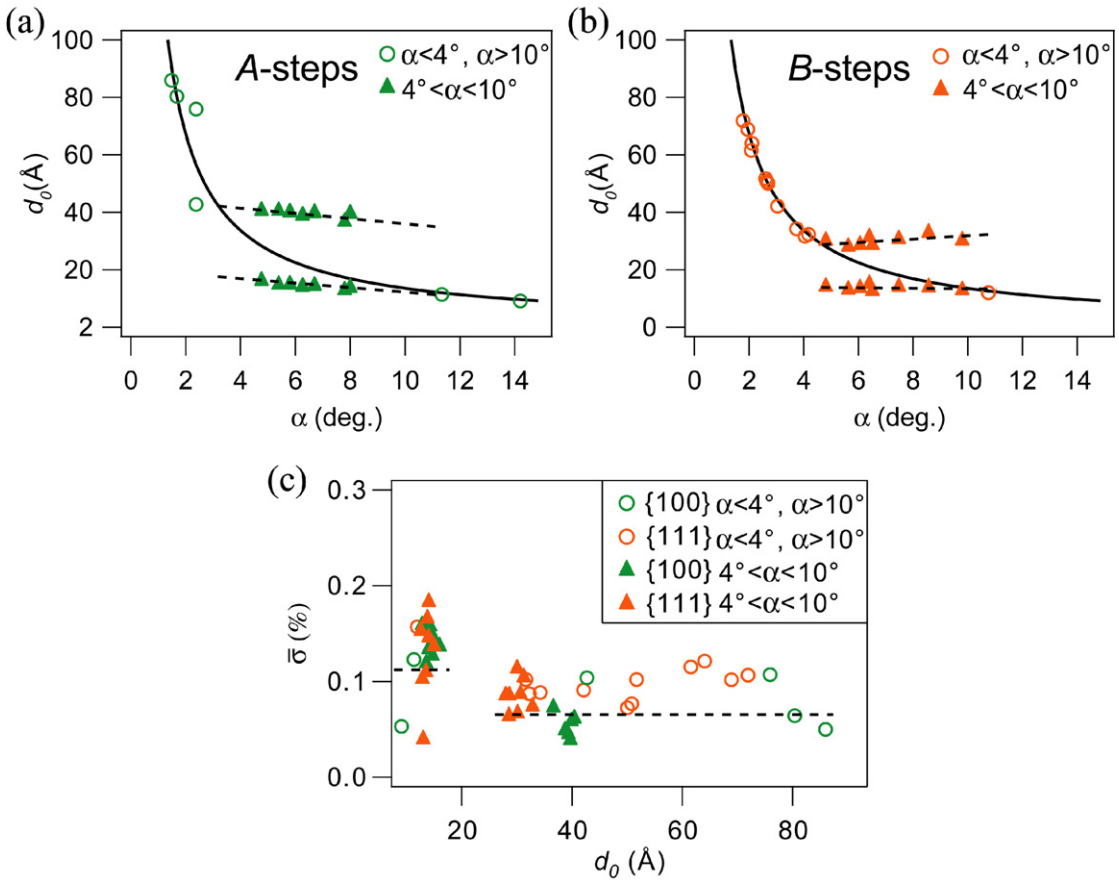

Figure 3. (a) and (b) Average terrace width d_0 measured at different miscut angles (α). Both quantities are determined from STM image analysis. In the ∼4°–10° faceting range, narrow (d_n) terraces maintain a value of ∼14 Å, while large (d_w) terraces range between ∼40 Å for A steps and ∼31 Å for B steps. The solid line represents the $d = h/\sin\alpha$ equation for a regular vicinal surface with monatomic steps. (c) Normalized terrace width distribution ($\bar{\sigma}$) plotted as a function of d_0, deduced from the same statistical analysis of STM images. Dotted lines mark the average $\bar{\sigma}$ values for d_w and d_n terraces.

part of the surface, the system exhibits a periodic hill-and-valley structure of ∼4° and ∼10° oriented minifacets, i.e. two different phases of relatively wide (d_w) and relatively narrow (d_n) terraces, respectively. As sketched at the top of figure 2, the periodic superstructure is different for A or B steps. For A-type steps, the d_w phase contains a single terrace whereas steps form bunches in the d_n phase. The 1D lattice is thus defined by a superlattice constant $D = d_w + m \times d_n$, where m depends on the local miscut ($m = 0$ at ∼4° and $m = \infty$ at ∼10°). At the B side, bunches of terraces are formed in both d_n and d_w phases, and hence the hill-and-valley periodicity D is much larger for the same miscut [8].

In both A and B sides faceting is driven by the characteristic herringbone reconstruction of the Au(111) plane [21], which is present in d_w terraces and absent in the d_n phase. Reconstructed and unreconstructed phases actually represent the two competing configurations of the system that give rise to structural instabilities and phase separation at certain miscuts [8]. The reconstruction of the terraces also leads to a complex atomic structure at step edges, which in turn results in rather different step energies at the d_w–d_n boundary in A or B sides [22]. The different phase boundary energy explains the dramatic variation of the faceting wavelength D from A- to B-type vicinals, shown in figure 2. For A steps, there is a little energy cost for inserting a d_w terrace inside a d_n bunch, and hence the system exhibits the maximum number of phase boundaries and the minimum periodicity D [23]. For B steps, the boundary energy is high and the system seeks the minimum number of boundaries, resulting in the largest size of the phases, and hence the longest period D.

The curved surface allows one to accurately determine the faceting range in Au(111) using STM. For this purpose we have carried out a detailed quantitative analysis of the terrace size across the curved Au crystal. The results are shown in figure 3, whereas figure 4 illustrates the analytical process carried out to analyze every STM image. The image analysis is performed on individual frames with sizes between 340 × 340 and 20 × 20 nm^2, like the one shown in figure 4(a). The automatic processing of individual STM images extracts the profile of each line scan and calculates the distance d between all the neighboring steps. This is repeated in different frames over a total area of 1 μm^2 for each α angle. All d values obtained for the same α (deduced from the average plane of the images) are then converted into a probability histogram, which is fitted with a Gaussian curve, as shown in figure 4(b). The mean value d_0 is given by the center of the fitted curve. The

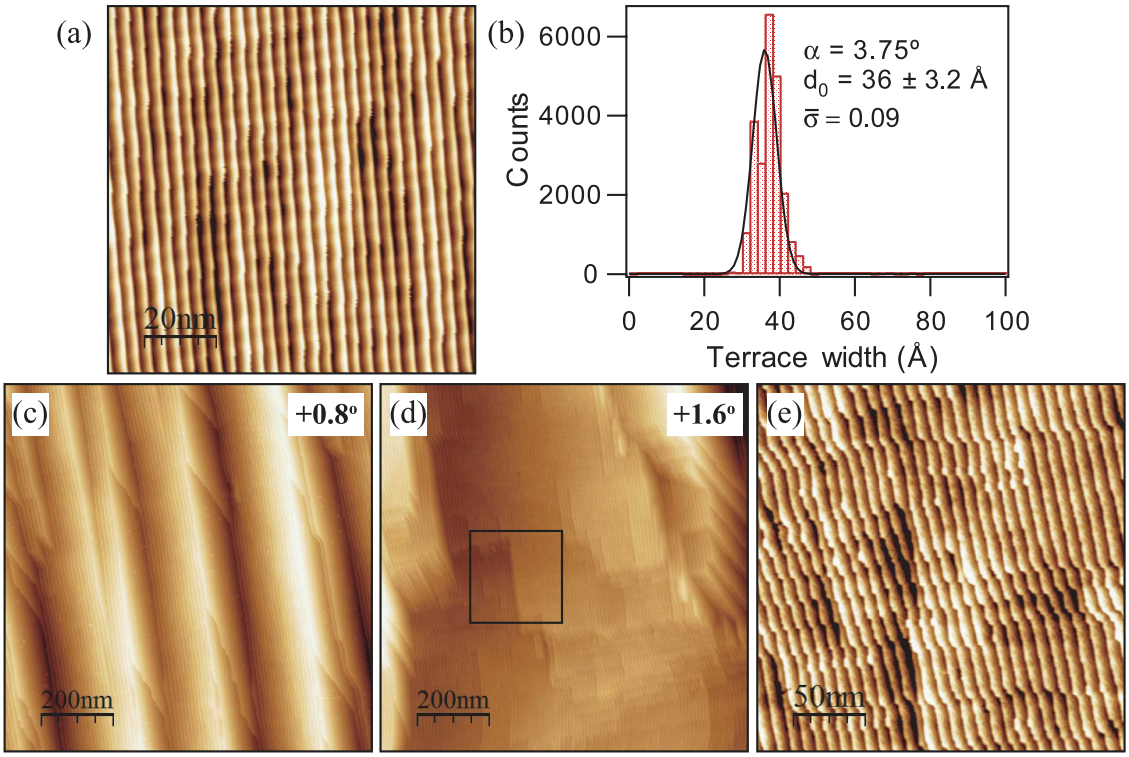

Figure 4. (a) Typical STM image used for the analysis in figure 3. It belongs to the B-type surface with 3.75° miscut angle. The analysis in panel (b) shows the distribution of 23 000 terrace widths calculated from the line profiles extracted in different images belonging to this surface. The terrace width distribution is fitted with a Gaussian curve (black) with center $d_0 = 36$ Å, $\sigma = 3.2$ Å and $\bar{\sigma} = 0.09$. (c)–(e) STM images displaying B-type surfaces with local miscut angle $\alpha = 0.8°$ and 1.6°. The image (e) is a zoom-in of panel (d), as indicated by the black square. In both sides of the sample, surfaces with $0.5° \leqslant \alpha \leqslant 2°$ miscuts are not well defined on a large scale (∼1 μm). Within such miscut range we find mixtures of large (111) terraces and irregular step arrays with varying sizes. These surfaces are discarded in the analysis shown in figure 3.

fit also renders the normalized terrace width distribution ($\bar{\sigma}$) defined as the ratio of the standard deviation of the Gaussian and d_0 [24]. The analysis is limited to surface areas exhibiting homogeneous step arrays in the 1 μm scale. This is the case of most surface areas with miscut angles above 2°, in both sides of the crystal. For $\alpha < 2°$, the curved surface exhibits inhomogeneous mixtures of large (111) terraces and irregular terrace arrays with different sizes (figures 4(c)–(e)) and hence STM data here are not analyzed.

Figures 3(a) and (b) show the average terrace size (d_0) as a function of the miscut angle (α) in A and B sides, respectively. For a regular step array, data must follow the expression for the lattice constant $d_0 = h/\sin\alpha$, which is represented by the solid line in both figures. At faceted areas, data points deviate from this curve, thereby delimiting the miscut range of faceting in Au(111) vicinals. It extends from 3.3° to 11° in A-type vicinals and from 4.6° to 10.6° in the B side. The horizontal dashed lines prove that, within the respective faceting ranges, d_w and d_n are almost constant values, in overall agreement with the STM analysis carried out by Rousset *et al* using a set of flat vicinal crystals [8]. In the B side we find $d_w = 31 \pm 3$ Å and $d_n = 13.5 \pm 1.0$ Å in the whole faceting range[5]. In the A side both d_w and d_n decrease slightly as a function of α, from $d_w = 41.0 \pm 1.5$ Å down to $d_w = 38.0 \pm 1.5$ Å and $d_n = 14.0 \pm 1.0$ Å to $d_n = 13.0 \pm 1.0$ Å.

In figure 3(c) we plot the terrace size distribution broadening $\bar{\sigma}$ as a function of d_0 for the full set of data. In general, we observe that relatively large terraces are sharply defined ($\bar{\sigma} \sim 0.07$), whereas data for small terraces are scattered around $\bar{\sigma} = 0.12$. We can also observe very low $\bar{\sigma} < 0.05$ values in large terraces of the A side, i.e. for $|\alpha| < 4°$. In such a low miscut range (below 4°), the A side frequently shows terrace sizes around $d_0 \sim 40$ Å and 80 Å. Moreover, at 2.4° we encounter a stable vicinal surface (see figure 2) that exhibits alternating bunches of terraces with 40 Å and 80 Å size, as predicted by Rousset *et al* [8].

In the standard elastic model $\bar{\sigma}$ can be expressed as a function of both the long-range step–step interaction strength and the so-called step stiffness [24]. Stiffer steps are static and straighter, while softer steps are mobile and distinguished by frizzy edges in STM images. On the other hand, the interaction strength depends on the stress energy of the terrace and the step dipole. These elastic properties vary when Au(111) terraces reconstruct. As shown in figure 5, d_w terraces larger than 30 Å exhibit fcc/hcp dislocation boundaries, which run either parallel (A side) or perpendicular (B side) to the steps. Such reconstructions, which are reminiscent of the $(22 \times \sqrt{3})$ herringbone that characterizes the Au(111) surface [21], disappear completely in small d_n terraces. Due to the presence

[5] d_w in the B side slightly differs from our recently published STM values [19], which were due to an improper calibration.

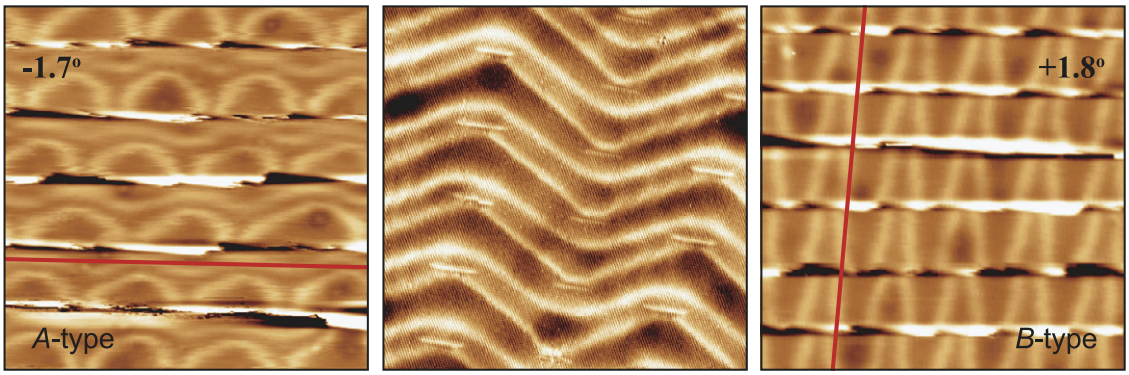

Figure 5. STM images (43×43 nm^2) showing the herringbone reconstruction on the (111) surface (center) and its transformation at A and B sides. The intensity is saturated at step edges, which appear as bright horizontal lines. On A-type vicinals (left, surface at $\alpha = -1.7°$) with terrace width $\geqslant$40 Å the discommensuration lines run parallel to the step edges, as indicated by the solid line. In contrast, on B-type vicinals (right, surface at $\alpha = +1.8°$) of terrace width $\geqslant$32 Å the reconstruction lines are perpendicular to the steps.

of hcp and fcc domains, the atomic arrangement of the step edges is different for d_w and d_n phases. In summary, all parameters that determine $\bar{\sigma}$, i.e. the step stiffness, the step dipole and the terrace stress are changing from reconstructed d_w to unreconstructed d_n phases. Therefore, one can naturally expect different $\bar{\sigma}$ values at both sides of the faceted range, as indeed proved in figure 3(c). However, $\bar{\sigma}$ is found to vary in a similar way (larger values for smaller terraces) in Cu(111) vicinal surfaces that show no terrace reconstruction. This is not contradictory with the Au(111) case, but rather points to the fact that the terrace reconstruction observed in Au(111) vicinals is not the reason but rather the particular consequence of a general property that may affect all vicinal surfaces, namely the variation of the elastic properties as a function of the miscut angle.

Vicinal surfaces with terrace reconstructions, such as the herringbone in Au(111), generally exhibit faceting instabilities [24]. As schematically plotted in figure 6, one can use the free energy curve of a vicinal surface to predict segregation of reconstructed d_w and unreconstructed d_n facets. The surface free energy is defined for both reconstructed and unreconstructed surfaces as a function of the α angle in the following way:

$$\gamma(\alpha) = \gamma_0 + \frac{\beta}{h}|\tan\alpha| + g|\tan\alpha|^3 \qquad (1)$$

where γ_0 represents the surface energy of the terrace, β the step energy and g the step–step interaction parameter. Making the reasonable assumption that γ_0 is lower for reconstructed d_w terraces, β lower for d_n steps, and that g is the same for both phases, then the free energy curves for reconstructed (γ_r) and unreconstructed (γ_{unr}) surfaces intersect at a critical α, as shown in figure 6. The phase segregation bypasses this critical miscut. The faceting angles $\alpha(d_n)$ and $\alpha(d_w)$ are determined by finding the maximum convexity of the lower envelope [8], i.e. by the tie line tangent to both curves depicted in figure 6. Conversely, using faceting angles as inputs one may estimate the differences in both γ_0 and β between d_w and d_n phases. Such differences fall in the meV/atom range, either for A and B faceting, as found by Rousset *et al* [8]. Therefore small

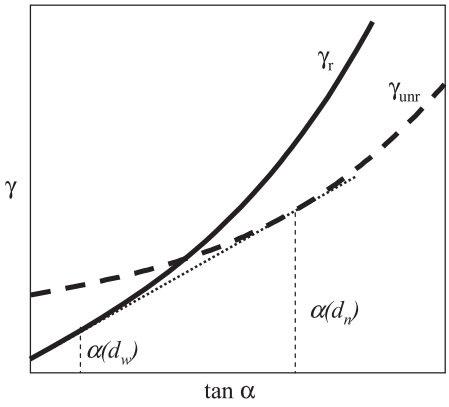

Figure 6. Surface free energy for reconstructed (solid curve) and unreconstructed Au(111) vicinals (dashed curve). Curves have been generated with equation (1) using, for the sake of clarity, arbitrary γ_0, β and g values. Phase segregation into d_w and d_n phases (dashed vertical lines) is predicted around the crossing point of the two curves following the tie bar construction (dotted line).

deviations from the constant elastic parameters assumed in equation (1) may determine new faceting angles. For example, the herringbone reconstruction in terraces defines magic sizes and hence additional surface energy minima [8]. One must also include non-elastic contributions to the surface free energy in equation (1), thereby altering the tie bar construction in figure 6. And finally, as we discuss below, the electronic energy adds fine ripples to the total $\gamma(\alpha)$ curve in figure 6, i.e. new convexity points that can modify the faceting range.

2.2. Evolution of electronic states across the curved Au(111) surface

In order to investigate the connection between surface states and faceting we have measured surface bands across the curved Au(111) crystal using ARPES. For laterally resolved ARPES, the size of the monochromatic synchrotron light is reduced along the $[1\bar{1}\bar{2}]$ direction to 100 μm, by means of the exit slits of the beamline. Given the curved shape of the surface, the light beam samples a small arc for a given α value, as sketched

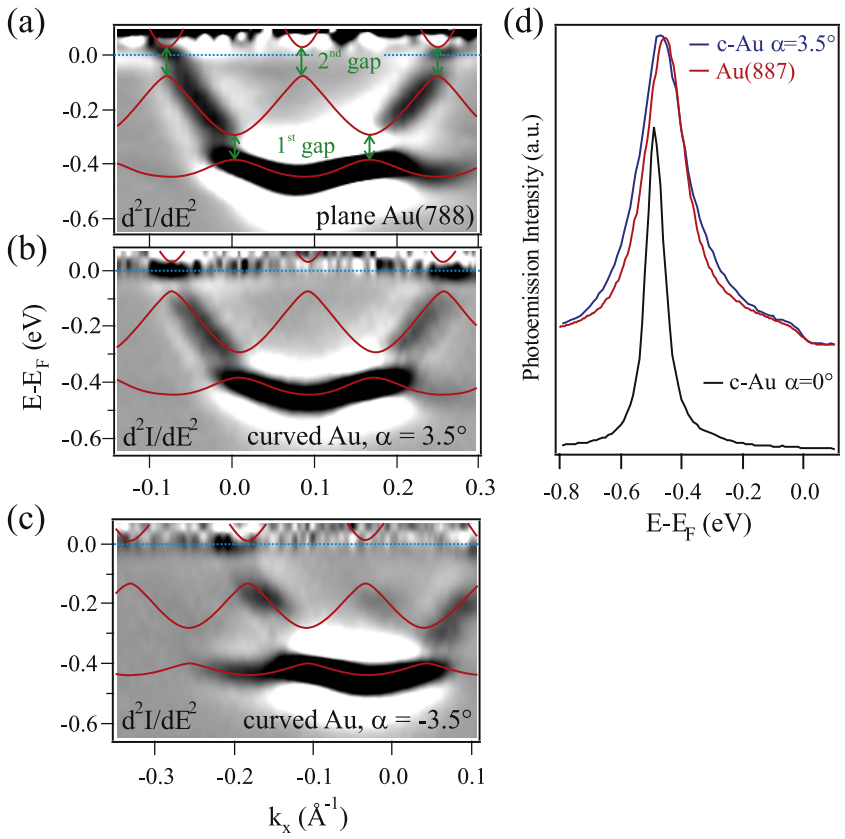

Figure 7. Surface state band measured with a photon energy of 21.2 eV for (a) a plane Au(788) and (b) and (c) the corresponding ±3.5° miscuts in the curved crystal. The second derivative of the photoemission intensity is displayed. Bands are fitted using a one-dimensional Kronig–Penney model (solid lines). (d) Photoemission spectra taken at the bottom of the surface band for Au(788) (red) and in the curved crystal (black, $\alpha = 0°$ and blue, $\alpha = 3.5°$). At $\alpha = 3.5°$ miscut, the spectrum in the curved sample is slightly broader than that in the flat surface, due to the finite sampling effect of the beam (see figure 1).

in figure 1. This defines an effective miscut broadening $\Delta\alpha \leqslant \pm 0.25°$ up to $\alpha \sim 8°$ that becomes somewhat larger at the edges of the crystal. $\Delta\alpha$ is therefore slightly larger than the accuracy achieved during mechanical polishing and Laue orientation ($\Delta\alpha < \pm 0.2°$). In figure 7 we test the lateral resolution of the ARPES experiment by comparing the surface state bands measured for a flat Au(788) crystal ($\alpha = 3.5°$) [2], and for the curved crystal at $\alpha = \pm 3.5°$ at B and A sides, respectively. The wavevector scale is referred to the center of the first Brillouin zone in the local (nominal) surface plane, i.e. $k_x = ((\hbar\omega - \Phi - E_B)2m/\hbar^2)^{1/2} \times \sin(\theta - \alpha)$, where $(\hbar\omega - \Phi - E_B)$ is the electron kinetic energy, m is the free-electron mass and θ is the emission angle with respect to the (111) direction. In order to enhance weak features, data are displayed as second derivative image plots in panels (a)–(c). In the (d) panel we compare the surface state spectrum at the bottom of the band in flat and curved surfaces. In (a)–(c) we find a complete equivalency, i.e. all bands exhibit the same topology. In figure 7(d) we detect a slightly broader peak for the curved crystal, as expected from the effectively larger $\Delta\alpha$ originated by the beam size. Taking this small difference into account, figure 7 generally demonstrates that the curved surface approach is valid to test surface states in vicinal surfaces using laterally resolved ARPES.

Surface bands of figures 7(b) and (c) are particularly important, since they belong to the lower onset of the faceting region at A and B sides. They show evident signatures of superlattice scattering, namely band folding with $2\pi/d$ vectors and small ∼0.1–0.15 eV energy gaps. The solid lines in figures 7(a)–(c) are fits to the bands using a Kronig–Penney model [1, 2]. In all cases, the fit places the first superlattice gap at $\sim E_F - 0.3$ eV and the second gap at E_F. As shown in the vicinal Cu(111) case [3], a Fermi gap can lead to a significant reduction in the electronic energy per surface atom compared to a non-gapped band. As we shall discuss later, Fermi gaps in figure 7 also introduce significant variations in the electronic energy as a function of α, which add to the total free energy in equation (1) and modify the tie bar construction in figure 6.

Figure 8 displays the evolution of the surface bands across the faceted portion of the curved sample. The photon energy is set to $h\nu = 42$ eV to better visualize step (d) and faceting (D) umklapps. In the top and bottom panels we observe the regular umklapps that characterize the 1D step arrays at upper and lower faceting onsets, i.e. free-electron-like bands folded with $2\pi/d_w$ and $2\pi/d_n$ umklapp vectors, respectively. Starting from the top panels, the faceted region is thus defined by a progressive build-up of the high energy d_n emission and the simultaneous quenching of the low energy d_w band. This behavior appears rather clear in B steps, where the large size of individual facets leads to an incoherent superposition of d_n and d_w bands. The surface bands in the faceted region of the A side look very different. We note the presence of a (progressively

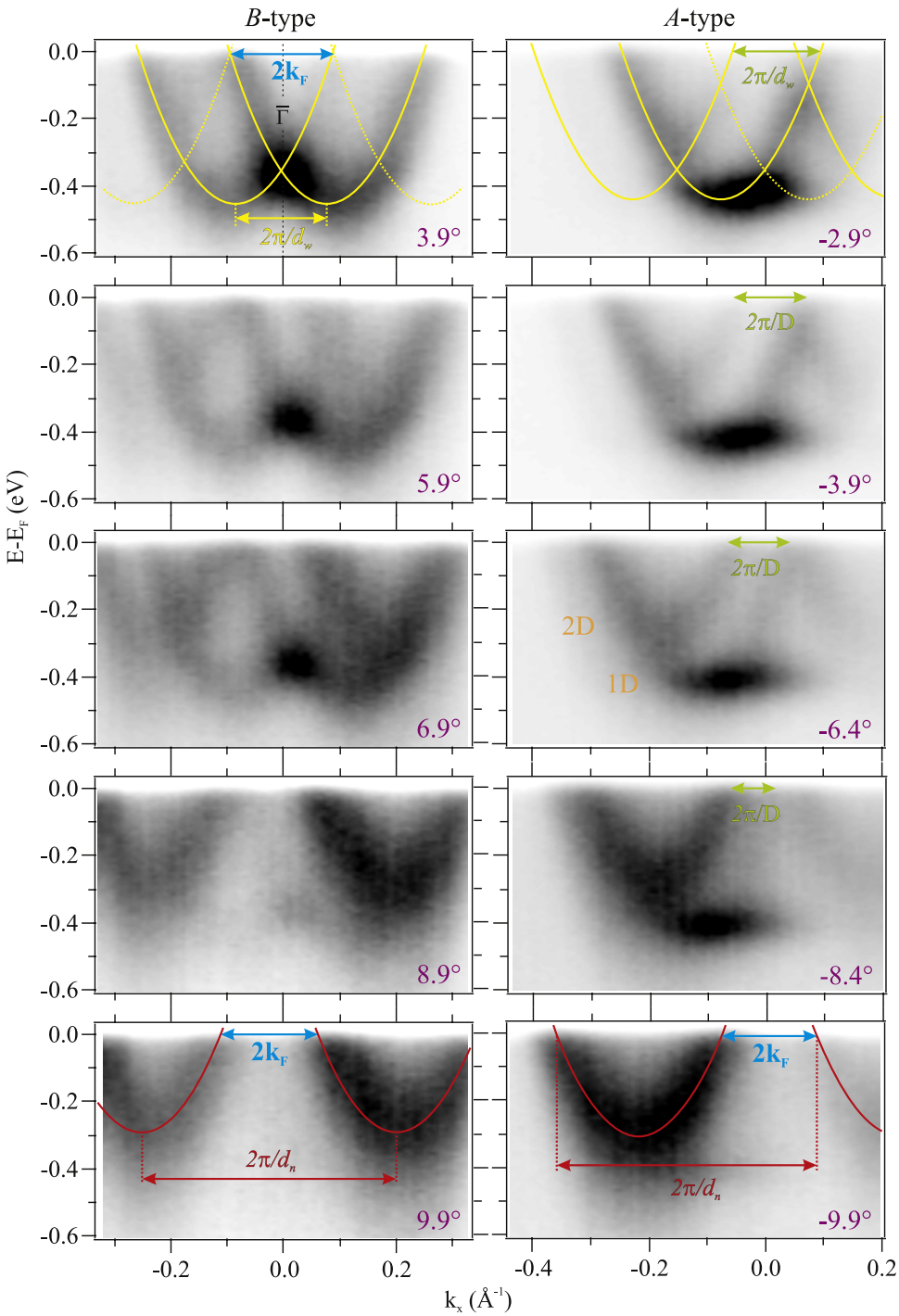

Figure 8. Surface bands across the faceted region of the curved crystal. Photoemission intensity maps correspond to the miscut angles indicated on the bottom right. k_X is the wavevector perpendicular to the step array on the local surface plane. On the B side (left panels), the spectrum smoothly evolves from d_w (top) to d_n (bottom) bands, with mixed contributions at intermediate miscuts. In the A side (right panels), the surface band splits into a quasi-1D state (low energy) and a 2D band (high energy). Solid lines are parabolic fits to d_w and d_n bands at the onsets of faceting. The dotted parabolas mark the position of second-order umklapps.

shrinking) $2\pi/D$ faceting umklapp, which smoothly evolves from the $2\pi/d_w$ step umklapp at the $-2.9°$ onset. The $2\pi/D$ umklapping proves the facet–superlattice character of surface states in the A side. Despite this superlattice nature, low and high energy features possess a dominating d_w and d_n character, respectively, as proved in a thorough spectral analysis of surface bands performed in a flat vicinal surface with A-type faceting [2]. In fact, as marked in the $-6.4°$ spectrum, we can single out a flat, quasi-1D band at ~ -0.4 eV, separated from the quickly dispersing 2D umklapp branches that cross E_F. As we shall discuss below, the lower energy, weakly dispersing feature belongs to a surface state with a large probability inside the d_w terrace, whereas the strongly dispersive bands that cross E_F have the dominant spectral weight located at d_n bunches.

Solid lines in figure 8 represent parabolic envelopes that fit d_w and d_n bands, respectively, at faceting onsets. d_w bands exhibit folding with $g_w = 0.185 \pm 0.015$ Å^{-1} and $g_w = 0.155 \pm 0.015$ Å^{-1} umklapp vectors in B and A steps, leading to $d_w = 34 \pm 3$ Å and $d_w = 41 \pm 3$ Å, respectively. Such values are slightly larger than those determined by STM in figure 3 ($d_w = 31$ Å and $d_w = 38$ Å, respectively). Although error bars in STM and ARPES values still overlap, there is a tendency to obtain smaller g values from ARPES umklapps due to the terrace size broadening [3], in particular with umklapps that lie too close, such as d_w bands. In contrast, the fit to umklapp bands in the lower panels of figure 8, which renders the same $g_n = 2\pi/d_n = 0.45 \pm 0.015$ Å^{-1} vector for A and B sides is in perfect agreement with the $d_n \sim 14$ Å value found by STM.

At the B side, with large d_w and d_n phases, we observe that both g_w and g_n are constant values in all spectra, reflecting the stability of d_w and d_n lattice constants across the faceting region proved in figure 3. The d_w umklapps in figure 8 appear nested at the Fermi energy with $4\pi/d$ superlattice vectors (dotted lines). This indicates that the second superlattice gap in d_w bands lies at E_F. Both first and second superlattice gaps can only be observed in second derivative images and using a lower photon energy, e.g. $h\nu = 21$ eV (figure 7), which provides better energy and momentum resolution. The arrows in figure 8 join folded parabolas at the Fermi energy defining the Fermi vector $2k_F$ for each phase. Since d_w bands are nested near E_F, then $2k_F \sim g_w$. Interestingly, d_n bands, which are not nested at E_F, exhibit a similar $2k_F = 0.180 \pm 0.015$ Å^{-1}. Thus, we may conclude that, within error bars, $2k_F \sim g_w = 2\pi/d_w$ is the same for both d_w and d_n phases of the B side.

Band minima in step bands lie at surface zone boundaries $\pm(n+1)/2 \times \pi/d$ [1], and hence the first Bragg reflection occurs at $\bar{\Gamma}$, i.e. $k_x = 0$. Such a nesting point is located below E_F for d_w bands (see figure 7) and above E_F for d_n bands (not visible). In order to shift the first Bragg reflection (and hence the first superlattice gap) to E_F, the lattice constant should be changed to $d \sim 16$ Å. This critical d value is similar for Cu(111) vicinals [3]. In the Au(111) curved surface the 16 Å terrace size, and hence the $\bar{\Gamma}$ nesting at E_F, is bypassed in the faceting transition. This phenomenon is nicely shown in figure 9(a), where we plot the Fermi level intensity measured with ARPES as a function of k_x and across the curved crystal. The k_x scale is referred to the nominal $\bar{\Gamma} = 2\pi/d$ symmetry point. The faceted regions are delimited with dotted lines. In the B side, the intensity maxima around $\bar{\Gamma}$ define a neck-like feature that reflects the jump from d_w to d_n bands with constant $2k_F$ vector. Due to faceting, $\pm\pi/d$ branches do not merge at $\bar{\Gamma}$, i.e. faceting prevents the collapse of the Fermi surface ($k_F = 0$). Interestingly, a similar $\bar{\Gamma}$ neck is observed in the A side as well, despite its different faceted superstructure (see figure 2). In this case the lack of intensity at $\bar{\Gamma}$ is explained by the physical nature of the 2D-like band that crosses E_F.[6] This is shown in the wavefunction model sketched in figure 9(b), which in turn is deduced from the photon-energy-dependent spectral intensity measured in ARPES [2]. The higher energy,

[6] The spectral intensity at $\bar{\Gamma}$ is entirely provided by the quasi-1D state of d_w terraces, but this lies well below the Fermi energy.

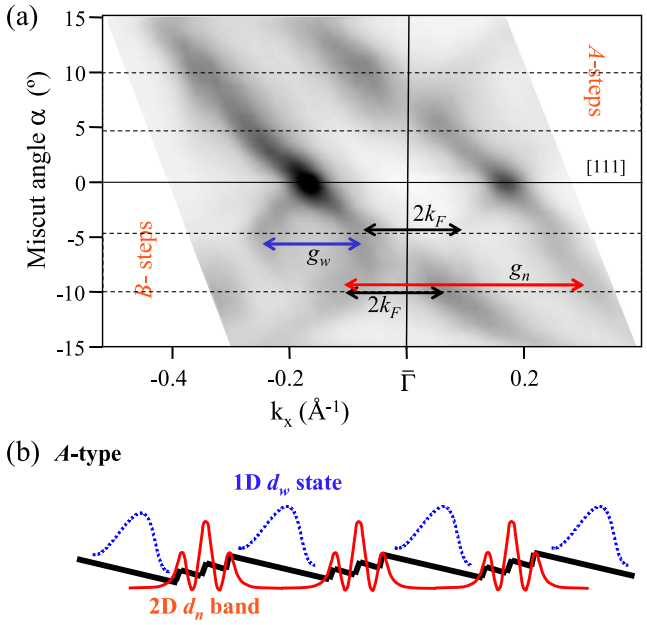

Figure 9. (a) E_F photoemission intensity map for the Au curved surface, as a function of α and k_x. The dashed lines mark the 4°–10° faceting range, which is characterized by a neck-like feature around $\bar{\Gamma}$ in both sides. In the B side this neck images the transition from d_w to d_n bands, skipping first zone nesting (see the text). In the A side, the neck reflects the minimum in the spectral density of the superlattice band that characterizes the faceted structure (see the text). (b) Wavefunction model for 1D and 2D states for A-type faceting, as deduced from the analysis of the spectral density map of surface states in A-type vicinals [2]. (See color figure online.)

2D state in A-type vicinals is only modulated at step bunches with the spatial frequency d_n. Therefore, we expect, across the whole A faceting range, spectral density maxima in E_F similar to those of d_n bands in figure 8, i.e. away from $\bar{\Gamma}$ and close to $\pm(n+1)/2 \times \pi/d_n$, thereby defining the $\bar{\Gamma}$ neck of figure 9.

3. Discussion

The apparent complexity of the surface band structure for the Au(111) faceted surfaces measured in figure 8 only stems from the particular geometry of the step array. This is proven by the photoemission intensity maps calculated in figure 10. Our theoretical model computes, within the dipole approach, the photoemission matrix element, or transition probability, assuming free-electron waves as final states and the Shockley surface state as the initial state [6]. For the final state, we take into account the phase of the photoelectron, which gives rise to diffraction due to the different heights of the terraces. On the other hand, the Shockley surface state is calculated using a model crystal potential along the perpendicular [111] direction (z direction). Parallel to the surface (x, y plane), we assume free-electron-like dispersion in the y direction and scattering by a periodic step lattice in the x direction, with barrier potentials $U_0 \times b$ located at step edges. $U_0 \times b$, the effective mass m^*, as well as the reference energy E_0 of the terraces (i.e. the minimum of the surface band for a surface without steps) are free parameters determined by fitting separately d_w and d_n bands at faceting onsets, i.e. in the top and

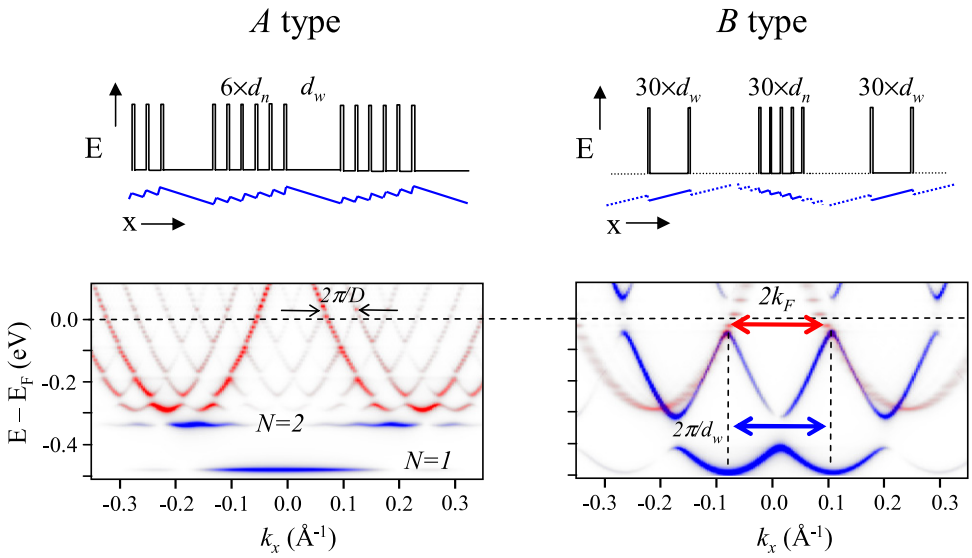

Figure 10. Calculated photoemission intensity maps for (a) A-type and (b) B-type faceted Au(111), using the finite systems respectively sketched on top, and 1 eV × Å barriers at step edges. Red and blue bands correspond to emission from d_w and d_n phases, respectively. In the A-type side, d_w bands are 1D QW states of the single d_w terrace, whereas d_n bands exhibit D umklapping. For B-type steps, the large size of the phases is enough to develop distinct d_n and d_w surface bands.

bottom panels in figure 8. The best fits are obtained using the same $U_0 \times b = 2$ Å × 1 eV barrier potential in all cases[7], $m^* = 0.27m_e$ (close to the value found for Au(111) [13]), and different $E_0 = -0.53$ eV and $E_0 = -0.42$ eV for d_w and d_n terraces, respectively. On top, we sketch the periodic step arrays calculated in each case. For the A side, we consider a periodic succession of six small $d_n = 14$ Å terraces and a single $d_w = 40$ Å terrace, i.e. a nominal miscut $\alpha = -7.5°$. For the B side, we assume 30 small $d_n = 14$ Å terraces embedded between two 30 × d_w facets, with $d_w = 34$ Å, i.e. $\alpha = +5.6°$. To clarify the nature of the different states we have systematically varied the relative proportion of d_w and d_n terraces in the array. This allows us to single out d_w and d_n features, which are plotted as blue and red bands, respectively.

The similarity of the model with the results in figure 8 is remarkable. The matrix element calculation modulates the intensity of the different branches in a way similar to that observed in the experiment, making the comparison between data and model more simple. This also allows us to further demonstrate the d_w or d_n nature of different band features in figure 8. In the A-side plot, D umklapping is rather clear, although only those bands around the main parabolic envelope appear more intense, as observed in figure 8. In the B-side calculation, both d_w and d_n phases are large enough to develop the separate bands observed in figure 8. The different type of faceting described in figure 2 is reflected in the distinct topology of the d_w-like (blue) states of figure 10. The large d_w phase at the B side exhibits dispersive behavior and d_w zone folding. In contrast, the single d_w terrace at the A side originates non-dispersing 1D quantum well levels below the d_n band, i.e. the $N = 1$ level at $E_B = 0.48$ eV, and the $N = 2$ that barely splits at the bottom of the 2D band at $E_B \sim 0.32$ eV. Note that the highly dispersive states that cross E_F in the A-side calculation of figure 10, left, have a spectral weight distribution similar to that of the fully developed d_n bands of the B side shown in figure 10, right, as expected from their same d_n nature. In particular, the spectral intensity maxima at E_F are located at the same k_x values in both figures. This explains the Fermi surface neck that characterizes the faceting range in figure 9(a), which in turn confirms the wavefunction model depicted in figure 9(b).

Given the success of the photoemission calculation to reproduce the ARPES data of figure 8, we can use it to investigate the possible influence of surface states and hence the electronic energy in the faceting transition. For $U_0 \times b$ and E_0 values that fit the data, the program can calculate the 2D surface band structure for smoothly varying step array configurations, which in turn can be integrated to obtain the corresponding electronic energy variation, and hence its possible influence in the free energy and tie bar construction of figure 6. We will discuss two different phenomena, first the electronic energy in the step lattice as a function of α, and second the electronic energy upon insertion of a single d_w or d_n terrace of varying size inside d_n and d_w bunches, respectively.

3.1. Fermi gap and electronic energy instabilities for $d = 34$ Å

Fermi energy gaps in step lattices are expected to influence the electronic energy of the system. Comparing gapped and ungapped bands with the same ground state energy (band minimum), a Fermi gap leads to a net electronic energy

[7] For the sake of simplicity, we have not taken into account the changes in step potential that arise as a function of the miscut [1]. Such barrier variations would not change the main conclusions of this work. However, a proper fit to the data does require an offset ΔE_0 from d_w to d_n terraces in both the A and B sides. This offset actually represents a change in the terrace energy E_0 from d_w to d_n terraces. Such a change in E_0 has not been considered in previous analysis of ARPES data in vicinal surfaces (see, for example, [1]), although it could be expected, given the important changes in elastic constants suggested from figure 3(c).

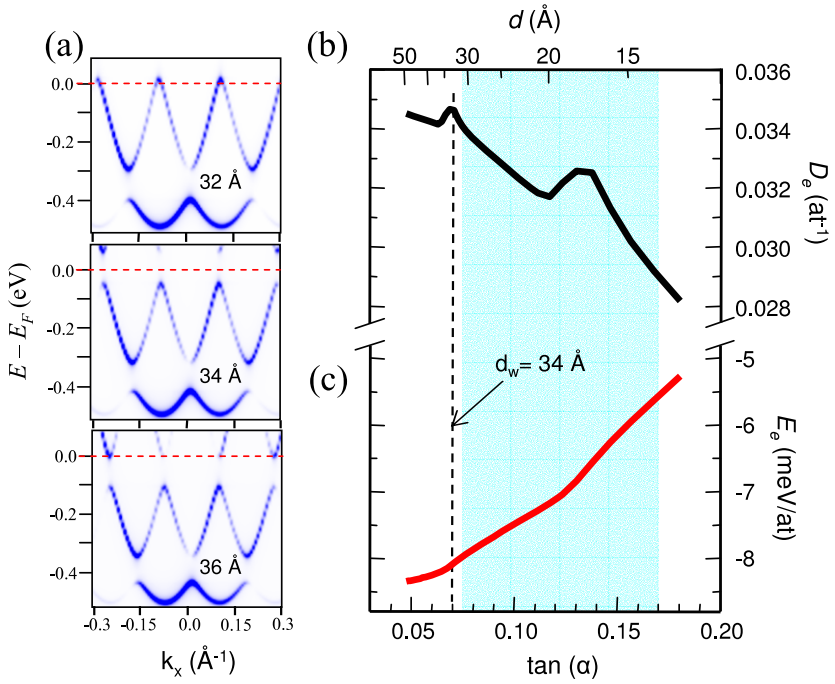

Figure 11. (a) Photoemission intensity maps calculated for step superlattices of varying d terraces. The second gap lies above and below E_F for $d = 32$ and 36 Å, and straddles E_F for $d = 34$ Å (middle panel). (b) Number of surface electrons per surface atom D_e and (c) electronic energy E_e calculated as a function of $\tan\alpha$ (bottom scale) and d (top scale). The shaded area marks the terrace size range that is never observed, due to faceting. Outside this range, the second Fermi gap leads to occupation maxima in D_e and inflection points in E_e around $d_w = 34$ Å.

gain [3]. However, such a comparison is not realistic, since the band bottom in the vicinal surface is shifted up due to repulsive scattering at steps. In other words, the energy reduction prompted by the Fermi gap in a vicinal surface is partly compensated by the upper shift of the surface band with respect to that in the (111) surface. One should instead study the electronic energy variation for vicinal surfaces with different lattice constant d. This is done in figure 11, where we calculate the band structure and the subsequent density of states D_e and electronic energy E_e for 1D step arrays of varying d, using the same step barrier $U_0 \times b = 1$ eV $\times$ 2 Å and terrace energy $E_0 = -0.53$ eV in all cases. In the three panels in figure 11(a) we illustrate the changes in the band structure for different d sizes. The second superlattice gap crosses the Fermi energy for $d = 34$ Å. Around this d value, we therefore expect changes in D_e and E_e of the system. These are represented in figures 11(b) and (c), respectively, as a function of the miscut $\tan(\alpha)$. The electronic energy E_e and the number of electronic states per surface atom D_e are numerically obtained using the following formulae:

$$D_e = \int_{E_0}^{0} N(\epsilon)\,d\epsilon; \qquad E_e = \int_{E_0}^{0} \epsilon N(\epsilon)\,d\epsilon \tag{2}$$

where $N(\epsilon)$ stands for the 2D density of states and ϵ for the electronic energy. The integral is performed in the 2D plane, i.e. bands are calculated for the 1D step potential array along k_x, whereas free-electron-like dispersion is assumed along k_y. In fact, the D_e curve in figure 11(b) exhibits occupation peaks at ∼4° and ∼7.5°, i.e. $d \sim 34$ Å and $d \sim 17$ Å, respectively. The latter represents the first superlattice gap crossing at E_F, although this never takes place due to the faceting transition (the faceted area of the crystal appears shaded in figure 11). The critical ∼4° and ∼7° points in D_e are mirrored in the E_e curve in figure 11(c) as small cusps in a growing function. To evaluate the impact of the electronic energy in the total free energy one can compare the average slope of the curve (ΔE_e) in figure 11(c) with the slope β/h of the linear term in equation (1). We find $\Delta E_e \sim 0.4$ meV Å^{-2}, which represents only ∼1% of β/h values in vicinal Au(111) [8]. However, the differences in the elastic constants between reconstructed and unreconstructed phases in B-type vicinals are extremely small ($\Delta\gamma_0 = 0.7$ meV Å^{-2} and $\Delta\beta/h = 5.3$ meV Å^{-2}, [8]), and hence little variations in β/h can considerably modify the tie bar of figure 6. Obviously ripples in the electronic energy are likely to influence a sensitive tie bar in B-type vicinals. In particular the ∼4° critical point in figure 11(c) should be reflected in the total free energy curve of figure 6 as a new convexity point that fixes the tie bar at this angle. Therefore we suggest that the electronic energy is the driving force that fixes, or simply favors, $d_w = 34$ Å in B-type faceting.

3.2. *QW split-off for $d_w = 37$ Å in A-type faceting*

As shown in figure 3, A-type faceted vicinals are defined by a single $d_w \sim 40$ Å terrace periodically inserted between $d_n = 14$ Å bunches. As discussed above, A-type vicinals possess a low step free energy that favors single terrace segregation, but the question arises why the terrace size should have such a particular $d_w \sim 40$ Å size. In A-type faceting one cannot

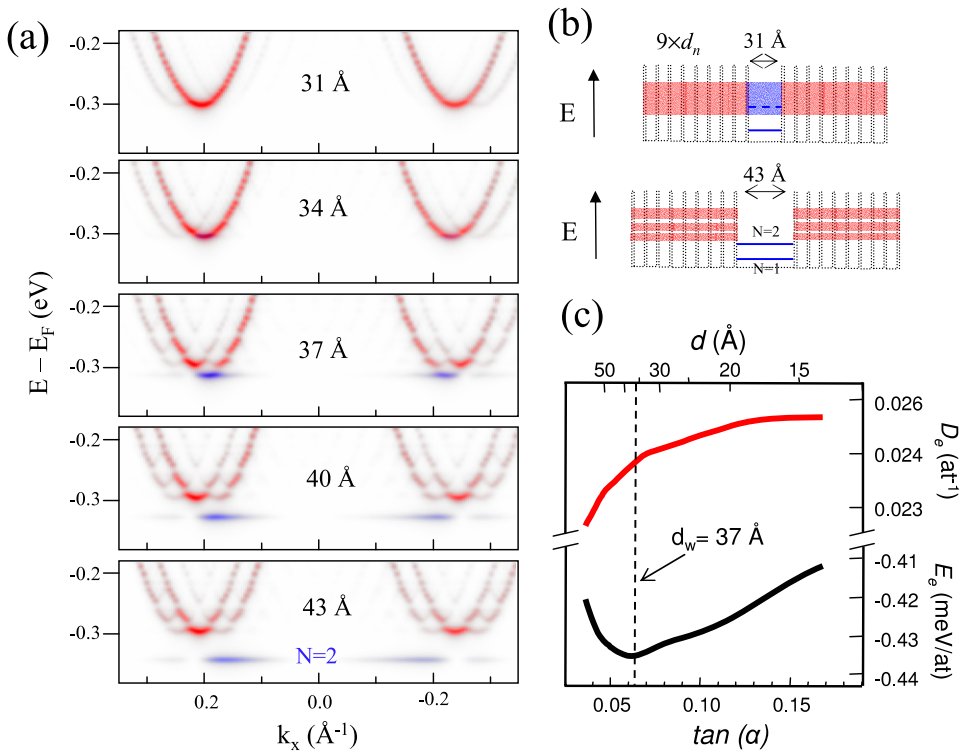

Figure 12. (a) Photoemission intensity maps calculated for the A-type faceted structure with a d_w terrace of varying size inserted between $(9 \times d_n)$ bunches ($d_n = 14$ Å). The second QW state splits from the bottom of the d_n band for $d_w > 37$ Å. (b) The drastic spectral intensity changes observed in d_n bands in the (a) panel are explained by the presence of coupling (decoupling) between d_n bunches for d_w values below (above) $d_w = 37$ Å. (c) Electronic energy E_e and occupation D_e calculated for a d_w terrace of varied size inserted between $(9 \times d_n)$ bunches ($d_n = 14$ Å), showing a critical point around 37 Å.

consider the electronic energy instability originated by Fermi gap opening in d_w bands, since d_w terraces do not form bunches. On the other hand, the elastic energy analysis for A-type Au(111) vicinals, including a Frenkel–Kontorova model to describe the surface reconstruction, does not predict any minimum or convexity point in the free energy curve at $d_w \sim 40$ Å [8, 22]. The particular $d_w \sim 40$ Å size in A-type steps could be linked to kinetic instabilities that arise during surface annealing and recrystallization. In fact, it has been shown that segregation of a terrace of critical size d_w can induce the nucleation of another such terrace nearby, and hence to the propagation of nucleation events [25]. If the local miscut is preserved, such a nucleation process can indeed explain the A-type faceted structure sketched in figure 2, i.e. the presence of periodic d_w terraces separated by d_n bunches with a total number of steps that depends on α. However, such a kinetic phenomenon would still not account for the specific $d_w \sim 40$ Å terrace width observed.

In figure 12(a) we show the band structure calculated for an A-type step lattice structure made of $(9 \times d_n)$ bunches ($d_n = 14$ Å) separated by single d_w terraces of variable size. The images display the energy range around the d_n band minimum (red), and hence the first ($N = 1$) QW-like level of the d_w terrace at -0.48 eV is not shown. For $d_w > 37$ Å one can notice drastic changes in the spectrum. The non-dispersing, $N = 2$ QW-like feature (blue) splits from the d_n-like band. The latter is also transformed from a single, smooth parabola for $d_w < 37$ Å into a set of minibands for $d_w > 37$ Å, which also exhibit a different spectral intensity distribution. Such a transition can be explained as due to the electronic decoupling between d_n bunches, as depicted in figure 12(b). If the $N = 2$ QW level overlaps the d_n bands, the former broadens and the latter are coupled from bunch to bunch, leading to a single extended state of the faceted structure. If the $N = 2$ state lies below the d_n band, d_n electrons are confined within decoupled bunches, leading to the series of broadened QW levels, i.e. the minibands observed for $d_w < 37$ Å in figure 12(a). The remarkable electronic structure and spectral intensity changes that accompany such $N = 2$ split-off are reflected in the electron occupation D_e and the electronic energy E_e of the system, as shown in figure 12(c). D_e exhibits a pronounced drop below 37 Å, probably due to the upwards shift (size effect within d_n bunches) experimented by the d_n band. Since the d_n band crosses E_F, an upwards shift leads to a net electronic energy gain, which explains the minimum in the E_e curve at 37 Å. Although the magnitude of the changes in E_e are very small compared to those in figure 11, these may be sufficient to create instabilities in the total free energy, thereby forcing the system to adopt the d_w size at the onset of the $N = 2$ QW state split-off that is observed in ARPES (figure 8).

3.3. Fermi energy crossing of QWs for $d_n = 14$ Å

The instabilities that arise in the electronic energy by segregating a particular d_w size inside a d_n bunch should also happen in the reverse case, i.e. for a single d_n terrace

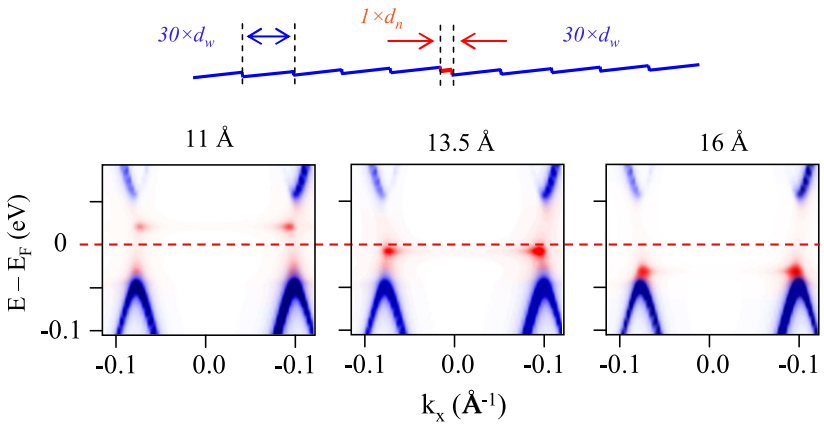

Figure 13. Photoemission intensity maps calculated for faceted structures with a varying d_n terrace inserted in a $d_w = 34$ Å lattice. The E_F gap supports a d_n QW, which becomes occupied around $d_n = 14$ Å.

segregated inside a d_w bunch. In such a case, the d_n terrace is the one characterized by discrete states, which may get confined inside d_w bandgaps. Let us consider a $d_w = 34$ Å lattice with E_F gaps. For d_n values around 14 Å the first QW shifts up to E_F, and hence inserting a $d_n \sim 14$ Å terrace inside the $d_w \sim 34$ Å bunch leads to QW confinement within the d_w bandgap around E_F. This is analyzed in figure 13, where we fix $d_w = 34$ Å and vary d_n. We can indeed observe the d_n QW state inside the Fermi gap for d_n values around 14 Å. Moreover, around $d_n = 14$ Å the QW state crosses E_F, thereby changing dramatically its occupation. Such 1D QW band depletion may affect faceting kinetics in the vicinity of the d_n terrace. In fact, surface electron removal eliminates the Ehrlich–Schwoebel barrier for atom diffusion across surface steps [26], which in turn speeds up interlayer mass transport. On the other hand, the occupation of the QW band (or the surface state) reduces the electronic energy, as shown in figure 11. Therefore, $d_n = 14$ Å appears to be a critical width at which instabilities may arise due to the competing kinetics (favored by QW band depletion) and surface energetics (favored by QW occupation).

4. Outlook: growth of nanostructures on curved surfaces

Vicinal surfaces are particularly attractive to achieve self-assembled arrays of lateral nanostructures such as stripes, wires and dots, which usually grow by step decoration during submonolayer growth [7–11]. Also, vicinal substrates are useful to obtain single-domain reconstructions or adsorbate phases that are difficult to single out on flat surfaces with high symmetry orientations [27–30]. However, growth on vicinal surfaces exhibit complex kinetics and energetics. For example, we expect anisotropic diffusion for adsorbates and step lattice matching restrictions for monolayers. The latter has been observed to prompt phase separation of well-matched adsorbate/substrate phases [31–33]. Therefore, in order to optimize a given adsorbate/vicinal system, the tunability of the substrate lattice constant d is highly desired. This can be readily achieved with a curved crystal surface.

In vicinal Au(111) surfaces step edges and terrace reconstruction patterns define a network for induced site-selective nucleation. It has been recently shown that highly regular arrays of metal dots or molecules grow on the vicinal Au(788) and Au(11 12 12) planes [7, 8, 34]. Using the curved Au(111) crystal we can explore the growth of quantum dots and molecular arrays by varying the step size across the sample. Figure 14 shows the STM images of the Co array formed after depositing 0.2 ML of Co onto the curved Au(111) crystal for two different miscuts. Co dots nucleate preferentially at the dislocations of the herringbone in Au(111) terraces, as shown in the center of figure 14. In B-type vicinals with reconstructed terraces it also nucleates at the crossing of the reconstruction lines and the step edges (figure 14, right panel), whereas in A-type vicinals they nucleate on terraces at arc-like herringbone lines (left panel). In both cases Co dots arrange forming rectangular patterns, whose dimensions can be tuned by changing the terrace width.

Adsorbates are generally expected to introduce significant changes in the electronic and elastic energy balance of the vicinal surface, and hence in its equilibrium morphology. Upon adsorption, vicinal surfaces often exhibit step bunching (or debunching) instabilities as well as a variety of faceting phases that depend on coverage (see, for instance, [27] and references therein). In figure 15 we analyze the case of Ag on vicinal Au(111), where the substrate faceting remains but the faceting structure changes. The curved crystal approach becomes again ideal to accurately track the change induced by the adsorption process in the equilibrium configuration of the system. Figure 15(a) shows the average terrace size measured with STM across the B side of the curved crystal, whereas (b)–(f) panels illustrate the characteristic morphology after 1 ML Ag deposition and annealing to 650 K. The annealing step is intended to accelerate the faceting kinetics and hence reach the equilibrium structure, although it gives rise to homogeneous Ag–Au surface alloying [35]. For the Ag-alloyed surface, the faceted range extends slightly below and above the critical angles of the clean substrate. The d_n phase remains a sharp 1D array with $d_n = 15.5 \pm 0.5$ Å, i.e. only about one atomic row larger than d_n in the clean substrate. In contrast, the d_w phase is significantly altered. After Ag adsorption and annealing,

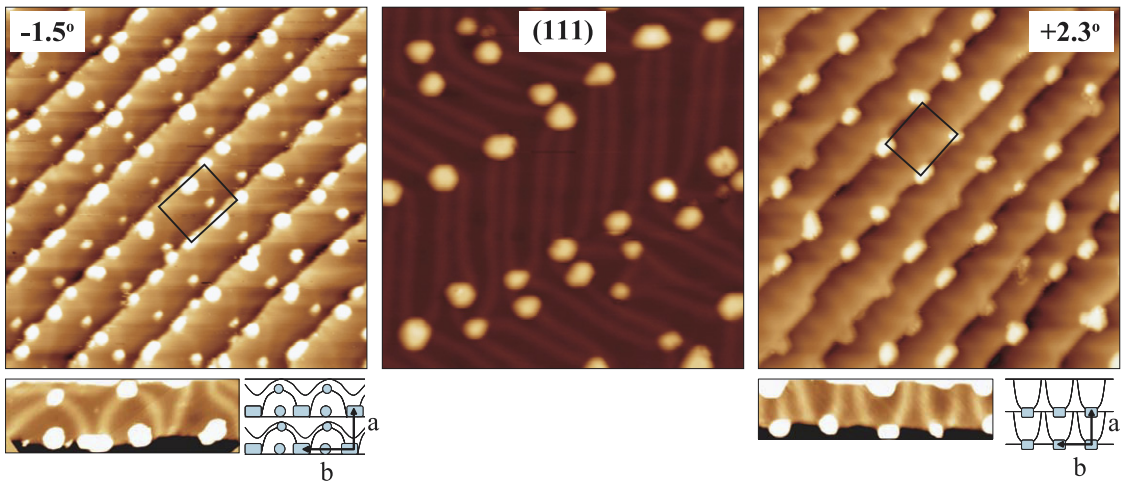

Figure 14. STM images (50×50 nm^2) of 0.2 ML Co grown at 170 K on the curved Au(111) crystal. On the (111) surface (middle) Co dots nucleate at dislocations of the herringbone lines (figure 5). On B-type steps (right) they grow at the crossing of the reconstruction lines and the step edges in fcc areas, while on wide (>75 Å) A-type terraces (left) they sit between step edges and arc-like herringbone lines, as pictured schematically in the bottom. In all cases they form rectangular lattices with periodicity (right) $a = 60 \pm 2$ Å, $b = 72 \pm 2$ Å and (left) $a = 85 \pm 2$ Å, $b = 95 \pm 2$ Å.

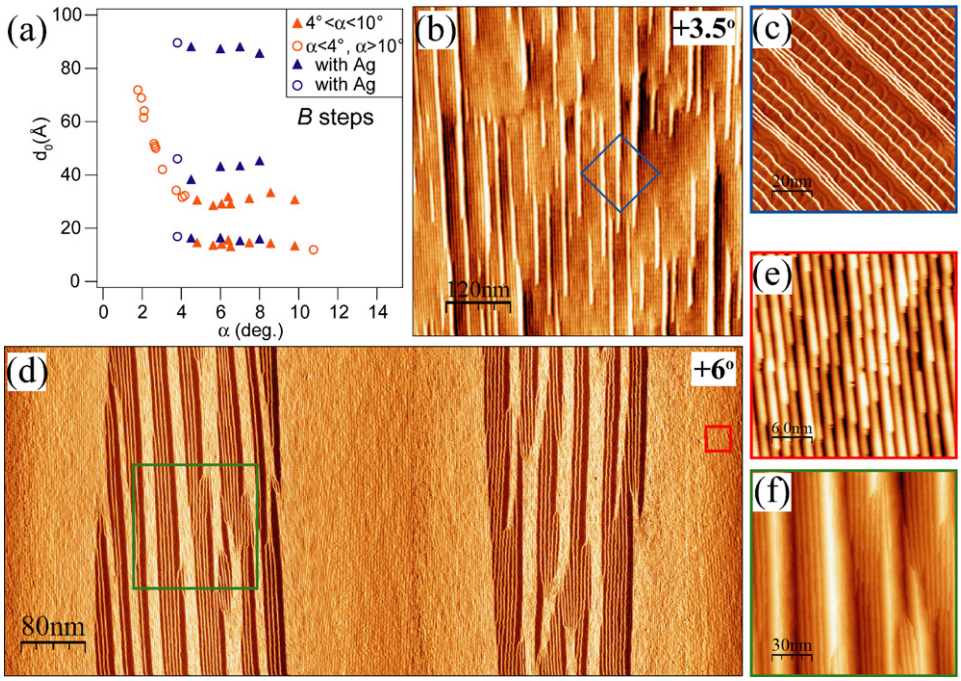

Figure 15. (a) Terrace width distribution of B-type steps estimated before (orange points) and after (blue points) the deposition of 1 ML of Ag and followed by a 10 min. annealing at 650 K. (b) and (c) STM images taken at $\alpha \sim +3.5°$ miscut, showing step disordering. (d)–(f) STM images taken at $\alpha \sim +7°$, illustrating the disruption of the step lattice only at d_w phase. (c), (e) and (f) are zoom-outs of the areas indicated in (b) and (d), respectively.

the d_w phase is made of a mixture of two terraces, with an average terrace size that has increased from ∼32 Å in the clean substrate (red data points) to 42 ± 3 Å (and also to 87 ± 1 Å) in the alloyed surface (blue data).

Figure 15(a) suggests the interplay between surface states and structure also for the alloyed surface. Note in figure 15(c) that the curved surface exhibits a terrace morphology, i.e. a herringbone reconstruction analogous to the one observed in the clean sample. This is due to the fact that Ag–Au alloying does not change the Au lattice constant [36]. We may therefore assume a relatively small change in elastic constants compared to the clean substrate, i.e. a minor change in terrace and step free energies for vicinal surfaces. On the other hand, Ag alloying in Au(111) leads to a small shift of the surface state band towards the Fermi energy, thereby reducing the Fermi vector k_F [37]. For step superlattices, a smaller k_F implies a shorter nesting vector $g_w = 2k_F$, i.e. a slightly larger critical terrace size $d_w = 2\pi/g_w$, exactly as observed in figure 15(a).

In conclusion, figure 15(a) points again to the influence of surface states in the faceted structure for the Ag-alloyed curved surface, although ARPES experiments to quantitatively prove such a connection are needed.

5. Summary

Using a curved crystal, we have explored the faceting transition that characterizes Au(111) vicinal surfaces. By means of STM image analysis we determined the terrace size distribution as a function of miscut, thereby delimiting the faceting range in Au(111). This extends over a wide interval of miscuts, but with fixed terrace widths d_w and d_n for each of the phases. Additionally, we studied the surface band structure by ARPES. The complex topology inside the faceting region can be understood on the grounds of a photoemission simulation, which proves the simplicity of the underlying physics, namely repulsive scattering of quasi-free-electron waves at step edges. Based on such photoemission simulations, we study the possible interference of the electronic energy in the free energy competition between reconstructed (d_w) and unreconstructed (d_n) vicinals. We indeed observe that critical terrace sizes correspond to Fermi energy gapping (d_w in B-type steps), 1D QW state split-off (d_w in A-type steps) and 1D QW state depopulation (d_n in A- and B-type steps).

Acknowledgments

We thank Javier García de Abajo for providing us with the codes used in photoemission calculations. The work is supported through projects of the Basque Government (IT257-07) and the Spanish Ministerio de Educacion y Ciencia (MAT2007-63083). The SRC is funded by the National Science Foundation (award no. DMR-0084402).

References

[1] Mugarza A and Ortega J E 2003 *J. Phys.: Condens. Matter* **15** S3281
[2] Mugarza A, Schiller F, Kuntze J, Cordón J, Ruiz-Osés M and Ortega J E 2006 *J. Phys.: Condens. Matter* **18** S27
[3] Baumberger F, Hengsberger M, Muntwiler M, Shi M, Krempasky J, Patthey L, Osterwalder J and Gerber T 2004 *Phys. Rev. Lett.* **92** 016803
[4] Baumberger F, Hengsberger M, Muntwiler M, Shi M, Krempasky J, Patthey L, Osterwalder J and Gerber T 2004 *Phys. Rev. Lett.* **92** 196805
[5] Didiot C, Fagot-Revurat Y, Pons S, Kierren B, Chatelain C and Malterre D 2006 *Phys. Rev.* B **74** 081404(R)
Malterre D, Kierren B, Fagot-Revurat Y, Pons S, Tejeda A, Didiot C, Cercellier H and Bendounan A 2007 *New J. Phys.* **9** 391
[6] Mugarza A, Ortega J E, Himpsel F J and García de Abajo F J 2003 *Phys. Rev.* B **67** 081404
[7] Didiot C, Pons S, Kierren B, Fagot-Revurat Y and Malterre D 2007 *Nat. Nanotechnol.* **2** 617
[8] Rousset S, Repain V, Baudot G, Garreau Y and Lecoeur J 2003 *J. Phys.: Condens. Matter* **15** S3363
[9] Kuhnke K and Kern K 2003 *J. Phys.: Condens. Matter* **15** S3311
[10] Pratzer M, Elmers H J, Bode M, Pietzsch O, Kubetzka A and Wiesendager R 2001 *Phys. Rev. Lett.* **87** 127201
[11] Tegenkamp C 2009 *J. Phys.: Condens. Matter* **21** 013002
[12] Bürgi L, Jeandupeux O, Hirstein A, Brune H and Kern K 1998 *Phys. Rev. Lett.* **81** 5370
[13] Reinert F, Nicolay G, Schmidt S, Ehm D and Hüfner S 2001 *Phys. Rev.* B **63** 115415
[14] Tosatti E 1995 *Electronic Surface and Interface States on Metallic Systems* ed E Bertel and M Donath (Singapore: World Scientific) p 67
[15] Silly F, Pivetta M, Ternes M, Patthey F, Pelz J P and Schneider W-D 2004 *Phys. Rev. Lett.* **92** 016101
[16] Schiller F, Cordón J, Vyalikh D, Rubio A and Ortega J E 2005 *Phys. Rev. Lett.* **94** 016103
[17] Ranke W, Xing Y R and Shen G D 1982 *Surf. Sci.* **122** 256
Ranke W and Xing Y R 1985 *Surf. Sci.* **157** 339
Kuhr H J and Ranke W 1987 *Surf. Sci.* **187** 98
[18] Kawakami R K, Escorcia-Aparicio E J and Qiu Z Q 1996 *Phys. Rev. Lett.* **77** 2570
Escorcia-Aparicio E J, Choi H J, Ling W L, Kawakami R K and Qiu Z Q 1998 *Phys. Rev. Lett.* **81** 2144
Choi H J, Kawakami R K, Escorcia-Aparicio E J, Qiu Z Q, Pearson J, Jiang J S, Li D and Bader S D 1999 *Phys. Rev. Lett.* **82** 1947
[19] Schiller F, Corso M, Cordón J, García de Abajo F J and Ortega J E 2008 *New. J. Phys.* **10** 113017
[20] Horcas I, Fernández R, Gómez-Rodríguez J M, Colchero J, Gómez-Herrero J and Baro A M 2007 *Rev. Sci. Instrum.* **78** 013705
[21] Harten U, Lahee A M, Toennies J P and Wöll Ch 1985 *Phys. Rev. Lett.* **54** 2619
[22] Repain V, Berroir J M, Croset B, Rousset S, Garreau Y, Etgens V H and Lecoeur J 2000 *Phys. Rev. Lett.* **84** 5367
[23] Marchenko V I 1980 *Sov. Phys.—JETP* **52** :129
[24] Jeong H-C and Williams E D 1999 *Surf. Sci. Rep.* **34** 171
[25] Jeong H-C and Weeks J D 1995 *Phys. Rev. Lett.* **75** 4456
[26] Memmel N and Bertel E 1995 *Phys. Rev. Lett.* **75** 485
[27] Kuntze J, Mugarza A and Ortega J E 2002 *Appl. Phys. Lett.* **81** 2463
[28] Crain J N, McChesney J L, Zheng F, Gallager M C, Snijders P C, Bissen M, Gundelach C, Erwin S C and Himpsel F J 2004 *Phys. Rev.* B **69** 125401
[29] Preinesberger C, Pruskil G, Becker S K, Dähne M, Vyalikh D V, Molodtsov S L, Laubschat C and Schiller F 2005 *Appl. Phys. Lett.* **87** 083107
[30] Fernández L, Löffler M, Cordón J and Ortega J E 2007 *Appl. Phys. Lett.* **91** 263106
[31] Fölsch S, Helms A, Zöphel S, Repp J, Meyer G and Rieder K H 2000 *Phys. Rev. Lett.* **84** 123
[32] Bachmann A R, Speller S, Mugarza A and Ortega J E 2003 *Surf. Sci.* **526** L143
[33] Ruiz-Osés M, González-Lakunza N, Silanes I, Gourdon A, Arnau A and Ortega J E 2006 *J. Phys. Chem.* B **110** 25573
[34] Néel N, Kröger J and Berndt R 2005 *Adv. Mater.* **18** 174
[35] Niemansverdriet J W, Market K, Dolle P and Wandelt K 1989 *J. Vac. Sci. Technol.* A **7** 2080
[36] Frenkel A I, Machavariani V Sh, Rubshtein A, Rosenberg Yu, Voronel A and Stern E A 2000 *Phys. Rev.* B **62** 9364
[37] Cercellier H, Fagot-Revurat Y, Kierren B, Malterre D and Reinert F 2004 *Surf. Sci.* **566–568** 520